

Observation of a Reconstructed Chern Insulator in Twisted Bilayer MoTe₂

Min Wu^{1,2*}, Lingxiao Li^{1*†}, Yunze Ouyang^{3*}, Yifan Jiang⁴, Wenxuan Qiu³, Zaizhe Zhang¹, Zihao Huo¹, Qiu Yang¹, Ming Tian⁵, Neng Wan^{5,8}, Kenji Watanabe⁶, Takashi Taniguchi⁷, Shiming Lei^{4†}, Fengcheng Wu^{3†}, Xiaobo Lu^{1‡}

¹International Center for Quantum Materials, School of Physics, Peking University, Beijing 100871, China

²Lab of Low Dimensional Magnetism and Spintronic Devices, School of Physics, Hefei University of Technology, Hefei, Anhui 230009, China

³School of Physics and Technology, Wuhan University, Wuhan 430072, China

⁴Department of Physics, Hong Kong University of Science and Technology, Clear Water Bay, Hong Kong SAR, China

⁵Key Laboratory of MEMS of Ministry of Education, College of Integrated Circuits Southeast University, Nanjing 210096, China

⁶Research Center for Electronic and Optical Materials, National Institute of Material Sciences, 1-1 Namiki, Tsukuba 305-0044, Japan

⁷Research Center for Materials Nanoarchitectonics, National Institute of Material Sciences, 1-1 Namiki, Tsukuba 305-0044, Japan

⁸State Key Laboratory of Surface Physics, Key Laboratory of Micro and Nano Photonic Structures (MOE), and Department of Physics, Fudan University, Shanghai, 200433, China

*These authors contributed equally.

Email: lilingxiaodh3111@pku.edu.cn, phslei@ust.hk, wufcheng@whu.edu.cn, xiaobolu@pku.edu.cn

Twisted bilayer MoTe₂ (tMoTe₂) is a prototypical moiré material in which long-wavelength superlattices amplify electron correlations, enabling a wealth of emergent quantum phases. To date, experimental efforts have focused primarily on small twist angles (typically $< 4^\circ$), whereas the larger-angle regime—where moiré bands become more dispersive and correlations are reduced—has remained largely unexplored. Here we chart the topological phase space of tMoTe₂ at a relatively large twist angle of approximately 4.54° , accessing a moderately correlated regime with enhanced bandwidth. In contrast to small-angle devices that predominantly host fractional quantum anomalous Hall or spin Hall responses, we uncover multiple Chern-insulating states with $|C| = 1$ at moiré fillings $\nu = -1, -0.53$ and $-1/2$. Strikingly, at $\nu = -2/3$ a magnetic field induces a fractional Chern insulator accompanied by an insulator–metal transition. Our results broaden the topological phase diagram of tMoTe₂ and establish large-angle moiré superlattices as a versatile platform for engineering robust topological states beyond the strong-correlation limit.

Main

R-stacked twisted bilayer MoTe₂ (tMoTe₂) has emerged as a model moiré platform for exploring correlated and topologically nontrivial phases of matter¹⁻⁴. At twist angles below 4°, a diverse set of quantum phases have been reported, including integer and fractional quantum anomalous Hall (IQAH, FQAH) states⁵⁻¹⁴, zero-field gapless composite Fermi liquid^{7,15}, fractional topological insulator^{16,17}, and unconventional superconductivity proximate to the FQAH state¹⁴, etc. These results point to an exceptionally rich correlated topological landscape in the strongly correlated regime of relatively narrow moiré bands. Because both the electron interaction strength and quantum geometry of the low-energy moiré bands are sensitive to the variations in the twist angle^{1-4,18-25}, a central question is how this landscape evolves when the moiré bands become more dispersive at larger twist angles, corresponding to a moderately correlated regime, which has remained largely unexplored experimentally. In this work, we address this regime by investigating the electronic properties of tMoTe₂ at a twist angle of approximately 4.54°. Transport measurements reveal several emergent phenomena, including electric-field-enhanced IQAH, previously unexplored QAH states at commensurate and incommensurate fillings, and magnetic-field-induced insulator-metal transition and re-entrant fractional Chern insulating state. Our results demonstrate a distinct, field-tunable regime of correlated topology beyond the strongly correlated limit.

Phase Diagram

We perform electrical transport measurements on dual-gated tMoTe₂ devices (schematically illustrated in Fig. 1a, See Method for details of the device fabrication). Figures 1c and 1d show the longitudinal resistance R_{xx} and the Hall resistance R_{xy} of device D1 as a function of filling ν and electric-field D/ϵ_0 at the base temperature $T = 10$ mK (unless otherwise specified, the data presented in this work are mainly collected on device D1), respectively. R_{xx} and R_{xy} are symmetrized and antisymmetrized under a small applied out-of-plane magnetic field $B = \pm 10$ mT to suppress accidental fluctuations. The moiré density is evaluated to be $n_M \approx 5.85 \times 10^{12}$ cm⁻² (one hole per moiré unit cell, $\nu = -1$), corresponding to a twist angle of approximately 4.54°, larger than those studied in previous works⁵⁻¹⁷. In this case, the phase diagram of the first moiré valence band can still be partitioned into two distinct regions: layer-hybridized region and layer-polarized region, which are separated by the tilted stripe regions (Fig. 1c). Within the layer-hybridized region, substantial R_{xy} approaching h/e^2 accompanied by vanishing R_{xx} ($< 50 \Omega$) emerges at $\nu = -1$ (Figs. 1c, 1d, as indicated by black dashed lines), a hallmark of IQAH state, where h and e are the Planck constant and elementary charge, respectively. These observations are consistent with earlier reports on tMoTe₂ with twist angles below 4°^{7,8,11-14}. Notably, the FQAH insulators at $\nu = -2/3$ and $-3/5$ ^{7,8,13,14} are absent, likely due to the dispersive band structure and non-uniform Berry curvature distribution at larger twist angles^{2,4,20-25}. Instead, at commensurate filling $\nu = -1/2$ and incommensurate filling $\nu = -0.53$ (as indicated by grey dashed lines in Figs. 1c, 1d), we observe large R_{xy} accompanied by R_{xx} minima (Extended data Fig. 6), indicative of topological non-trivial states that spontaneously break time-reversal and

translational symmetries. In the layer-polarized region, several topologically trivial correlated insulating states are identified at $\nu = -1, -2/3, -1/2, -1/3$ and $-1/4$ (Fig. 1c and Extended Data Fig. 3).

Collapsed IQAH state near zero electric field at $\nu = -1$

We first examine the characterization of IQAH state at $\nu = -1$. Figure 1e shows R_{xy} and R_{xx} as a function of the magnetic field around $\nu = -1$ at $D/\epsilon_0 = 0.15$ V/nm and $T = 10$ mK. Both the maximum of R_{xy} and minimum of R_{xx} vary linearly with the applied magnetic field down to zero, yielding a Chern number $|C| = 1$ according to the Streda formula $C = \Phi_0 \partial n / \partial B$ (indicated by the white dashed lines), where Φ_0 is the magnetic flux quantum. The zero-field Hall resistance remains quantized up to 2 K, accompanied by the small longitudinal resistance and pronounced magnetic hysteresis loops, indicative of robust ferromagnetic order, as depicted in Fig. 1f. At higher temperatures, the Hall resistance R_{xy} gradually deviates from the quantization, and the corresponding R_{xx} begins to surge sharply. Based on the temperature dependence of R_{xy} and R_{xx} (Fig. 1f), the Curie temperature is estimated to be about 6 K at $\nu = -1$, smaller than that obtained in earlier works^{7,8,11-14}, likely originating from the weaker interaction strength at the larger twist angle.

Notably, the stability of the IQAH state exhibits a counterintuitive dependence on the out-of-plane electric field. As the electric field approaches zero, the range of filling factors (ν) over which the IQAH state is observed narrows (see Figs. 1c and 1d). A similar electric-field-dependent suppression of the topological state is also observed in device D2, although without clear Hall quantization (Extended Data Fig. 1b). To further elucidate this behavior, we plot the electric-field-dependent IQAH state across various filling factors in Extended Data Fig. 4. Figure 2a plots R_{xx} and R_{xy} versus D/ϵ_0 at $\nu = -1$. At $T = 10$ mK and zero electric field, R_{xy} exhibits a slight deviation from perfect quantization, accompanied by a marginal increase in R_{xx} to $\sim 200 \Omega$. Nevertheless, the values remain well within the IQAH effect framework compared with previous literature benchmarks^{7,8}. By contrast, upon raising the temperature to 1.2 K, deviations from quantized Hall resistance become more pronounced, indicating the reduced robustness of IQAH state at zero electric-field limit.

The collapse of IQAH state reflects a reduction of incompressible gap with D/ϵ_0 . To quantify this effect, we examine the temperature dependence of R_{xx} and R_{xy} at selected electric fields, as shown in Fig. 2b. From the onset of IQAH effect breakdown, we extract the effective incompressible gap as a function of electric field in Fig. 2c (See Extended Data Fig. 5 for details). Although the magnitude of gap determined from R_{xx} and R_{xy} is different, both reveal the same nonmonotonic evolution with electric field: the gap increases from 1.8 K at zero electric field to a maximum of 11.3 K at 0.154 V/nm and subsequently decreases to 5.2 K at 0.253 V/nm for R_{xx} case. Notably, as shown in Fig. 2b, R_{xy} decreases monotonically with increasing temperature, evolving from a quantized value towards zero, whereas R_{xx} initially displays nonlinear rise, peaks near temperature where $|dR_{xy}/dT|$ is maximal, and subsequently undergoes a resistive

state-to-metal transition as evidenced by a sign change in dR_{xx}/dT . The nonmonotonic temperature dependent R_{xx} is phenomenologically reminiscent of the Kondo-like transport behavior²⁶⁻²⁹, but present data cannot verify the Kondo mechanism. Such a clear Chern insulator-resistive state-metal transition has not been previously reported in tMoTe₂, and calls for further theoretical investigations to reveal the microscopic origin.

Both the collapse of the IQAH state stability window and the nonmonotonic gap variation sharply contrast with the behaviors observed in tMoTe₂ devices with twist angles below 4°, where the $\nu = -1$ IQAH state remains robust near zero electric fields^{7,8,11-14}. In contrast to the smaller twist angle devices in the strongly correlated regime, the moiré bands at larger twist angles are more dispersive, leading to a more pronounced variation in the density of states (DOS). As shown by the calculated single-particle DOS at a twist angle of 4.54° (Fig. 1b), as the interlayer potential difference $|U_z|$ decreases, the van Hove singularity (vHS), where the DOS diverges, shifts continuously from $\nu < -1$ to $\nu > -1$. Therefore, the vHS crosses the $\nu = -1$ at finite electric fields, coincident with the enhancement of the Curie temperature, as Stoner ferromagnetism is strengthened by the increase in the DOS. Similar enhancements of correlated insulators through field-tunable vHS have been observed in twisted bilayer WSe₂, although the insulators in that system are topologically trivial^{30,31}.

IQAH states at $\nu = -1/2$ and $\nu = -0.53$

We next investigate the previously unexplored topological states at fillings $\nu = -1/2$ and $\nu = -0.53$, which manifest as pronounced maxima in R_{xy} accompanied by minima in R_{xx} (Figs. 1c, 1d and Extended data Fig. 6). To further explore the topologically nontrivial properties of these two states, R_{xx} and R_{xy} versus ν and B at $D/\epsilon_0 = 0$ and $T = 10$ mK are presented in Figs. 3a and 3b, respectively. In addition to the $\nu = -1$ state, which exhibits a slope corresponding to a Chern number $|C| = 1$ (white solid lines), the $\nu = -1/2$ state displays a similar linear shift in the ν - B maps down to zero magnetic field, yielding the same Chern number $|C| = 1$ according to the Streda formula (white dashed lines). This observation is distinct from the physics reported in smaller twist angle systems ($< 4^\circ$), where the $\nu = -1/2$ state appears to be a gapless composite Fermi liquid behavior^{7,15}. The emergence of an integer Chern number at a commensurate fractional filling points to the interaction-driven quantum anomalous Hall crystal (QAHC), also known as topological charge density wave, stabilized by spontaneous breaking of translational symmetry^{23,32-35}. To theoretically elucidate this state, we perform exact diagonalization (ED) calculation at filling $\nu = -1/2$, assuming spontaneous full spin polarization. We find four quasi-degenerate many-body ground states separated by a finite gap from excited states (Fig. 3g), with momentum indices consistent with a charge density wave state (Fig. 3h). Under twisted boundary condition, we evaluate the many-body Chern number and find that each of the quasi-degenerate ground states carries $|C| = 1$, in agreement with the observed IQAH transport signatures. The real-space hole density (Fig. 3i), calculated for a state that is a linear superposition of the four quasi-degenerate many-body ground states pinned by an attractive impurity potential, exhibits a

pronounced 2×2 charge modulation. The maxima are located on one out of four MM sites (i.e., the high-symmetry sites where the metal atoms are vertically aligned) within the moiré superlattice, providing direct evidence for the crystalline order. Thus, the IQAH state observed at $\nu = -1/2$ is compatible with the QAHC scenario, consistent with the theoretical proposal for tMoTe₂²³. This topological phase has also been experimentally observed in rhombohedral pentalayer graphene and twisted bilayer–trilayer graphene^{36,37}, but has not, to our knowledge, been revealed previously in semiconductor moiré superlattices^{7,8,11-14}.

While R_{xy} is not fully quantized to h/e^2 with a finite R_{xx} (~ 2 k Ω , Extended Data Fig. 6) under zero magnetic field at $\nu = -1/2$, it acquires $\sim 97\%$ quantization under a small magnetic field of $|B| = 10$ mT, and exhibits evident hysteresis loop, as shown in Fig. 3c. This suggests incomplete suppression of dissipative channels of our device, which likely arises from limited bulk mobility, local strain or twist angle inhomogeneity rather than the absence of underlying topological order. The QAHC state remains stable up to ~ 250 mK, above which the anomalous Hall response gradually deviates from quantization (Figs. 3c and 3d), while the ferromagnetic order persists to a Curie temperature of $T_c \approx 1.5$ K.

Upon slight hole doping beyond $\nu = -1/2$, an additional topological phase occurs at the incommensurate filling $\nu = -0.53$ (Fig. 3e), and this phase exhibits an anomalous magnetic field dependence (Figs. 3a, 4a, 4b, 4e, and Extended Data Fig. 6). In contrast to $\nu = -1$ and $\nu = -1/2$, neither R_{xx} minimum nor R_{xy} maximum displays a well-defined linear dispersion in ν – B map at $\nu = -0.53$. A linear fit of the R_{xx} minimum trajectory at small magnetic fields, when interpreted via the Streda formula, would indicate an effective Chern number substantially larger than $|C| = 1$ (Extended Data Fig. 6). Despite this unconventional field dependence, a quantized R_{xy} ($\sim 0.99 h/e^2$) with $R_{xx} \sim 1$ k Ω under $|B| = 10$ mT and $T = 10$ mK is observed, as shown in Fig. 3e and Extended Data Fig. 6. Such behavior at an incommensurate filling is reminiscent of the re-entrant IQAH effect at $\nu = -0.63$ in 3.83° tMoTe₂¹⁴, the extended QAH effect in rhombohedral multilayer graphene³⁸, and the re-entrant integer quantum Hall effects in high-mobility two-dimensional electron gases at high magnetic fields^{39,40}. This incommensurate IQAH state persists up to ~ 150 mK, whereas the associated ferromagnetism disappears near $T = 1$ K. Given that the QAHC states are theoretically explored predominantly at commensurate fractional fillings^{23,32-35}, the emergence of QAH state with anomalous magnetic field dependence at incommensurate filling suggests a different microscopic mechanism (beyond the scope of present work) that warrants further theoretical and experimental explorations.

Magnetic-Field-Driven Phase Transition at $\nu = -2/3$

Figures 4a and 4b show the ν – D/ϵ_0 maps of R_{xx} near $\nu = -2/3$ at different magnetic fields and base temperature $T = 10$ mK (the corresponding R_{xy} is shown in Extended Data Fig. 7). The resistance peaks emerging in the range 0.114 V/nm $< D/\epsilon_0 < 0.167$ V/nm (Fig. 1c) of the layer-polarized regime are strongly suppressed (Fig. 4a) and completely

annihilated (Fig. 4b) at $|B| = 0.25$ T and 1 T, respectively. This magnetic field driven evolution is further illustrated in Fig. 4c, which plots R_{xx} against ν and B . The resistance peak diminishes continuously as the magnetic field increases and disappears beyond ~ 320 mT. A similar phenomenon is observed upon increasing temperature, indicative of a melting behavior (Extended Data Fig. 7). From the temperature dependence of longitudinal resistance, we extract the energy gap by fitting the data to the Arrhenius equation at various magnetic fields (Fig. 4d), which displays a significant suppression with increasing the magnetic field. These observations suggest that the correlated insulating state at $\nu = -2/3$ sharply contrasts to the conventional expectation for charge density wave order, which is typically stabilized by magnetic fields^{41,42}. Instead, this anomalous magnetic response may arise from local magnetic scattering, potentially due to spin fluctuations^{12,13} or the Kondo-like physics²⁶⁻²⁹.

At higher magnetic fields, a new phase emerges near $|D/\epsilon_0| = 0.1$ V/nm within the layer-hybridized regime, characterized by a small R_{xx} accompanied by a large R_{xy} , as shown in Figs. 4e and 4f, indicative of a magnetic field induced topologically nontrivial state. A linear dispersion originating from $\nu = -2/3$ is identified according to the Streda formula, giving rise to a Chern number $|C| = 2/3$, as denoted by the black dashed line in Fig. 4g (the corresponding R_{xx} is plotted in Extended Data Fig. 7). This topological state bears close resemblance to the re-entrant IQAH effect observed in 3.83° tMoTe₂¹⁴. However, in comparison to the zero-field quantized counterpart at smaller twist angle, the present re-entrant state remains imperfectly quantized even under the magnetic field up to 4 T (Fig. 4h). The Chern number of this re-entrant topological state is $|C| = 2/3$ according to the Streda formula, rather than $|C| = 1$ (Extended Data Fig. 7), indicates a putative fractional Chern insulating state, reminiscent of that observed in graphene moiré systems⁴³.

Discussion and Conclusion

Our results uncover distinct correlated topological phase diagram in 4.54° tMoTe₂, deviating from the established phenomenology at smaller twist angles⁵⁻¹⁷. The nonmonotonic electric field dependence of $\nu = -1$ IQAH gap underscores the importance of vHS in strengthening topological states in the moderately correlated moiré bands, suggesting that engineering the alignment between the chemical potential and divergent DOS in topologically nontrivial bands provides a promising strategy for enhancing topological phases. The emergence of unconventional topological states at $\nu = -1/2$ and $\nu = -0.53$, as well as the magnetic field assisted re-entrant topological state at $\nu = -2/3$, demonstrates that the topological physics is reshaped at moderately correlated regime compared to the strongly correlated regime.

In conclusion, we have mapped the electronic phase diagram of tMoTe₂ at twist angle of approximately 4.54° , unveiling a rich landscape of interaction-driven topology, in which commensurate and incommensurate fillings host different correlated topological states. These findings underscore the importance of twist angle and band structure engineering in realizing robust and diverse quantum phases in semiconductor moiré

superlattices. Future experiments combining local scanning probes with transport measurements will be essential to directly visualize the translational symmetry breaking of the QAHC state and verify magnetic field assisted re-entrant fractional Chern insulator.

Note: A recent study of twisted monolayer-bilayer MoTe₂ at a twist angle of 3.7° reported similar phenomena, including a QAHC at $\nu = -1/2$ and an incommensurate IQAH state near $\nu = -0.53$ ⁴⁴.

Methods

Device Fabrication

Hexagonal boron nitride (hBN), graphite and 2H-MoTe₂ (HQ) flakes were exfoliated from bulk crystals onto 285 nm SiO₂/Si substrates with the thickness determined by optical contrast and atomic force microscopy (AFM). The tMoTe₂ devices with local contact gate were fabricated using dry-transfer and “cut and stack” method⁷. The bottom gate was prepared by picking up a hBN flake (thickness 10–15 nm) and a few-layer graphite flake using polycarbonate/polydimethylsiloxane stamp, then released onto the SiO₂/Si substrate at a temperature of 180 °C. Contact electrodes Pt (~ 8 nm) were patterned into Hall-bar configuration by standard electron beam lithography (EBL) and e-beam evaporation, followed by annealing at 350 °C for 3 hours and cleaning under AFM contact mode to remove the residue. To prevent oxidation or degradation, the tMoTe₂ structure was fabricated in a glovebox with O₂ and H₂O concentrations below 0.1 ppm. A MoTe₂ monolayer was cut into two parts by AFM tip or laser and sequentially picked up by a thin hBN (~ 5 nm) with a twist angle of 4.54°. The finished stack was released onto Pt electrodes at 180 °C. A local Pt contact gate (~ 8 nm) was deposited on the thin hBN above the contact electrodes to obtain a heavy doping and reduce the contact resistance, which was cleaned by AFM again. The top gate made of graphite/hBN (~ 10 nm) was fabricated to complete the transfer. Next, Cr/Au (5/60 nm) contacts were evaporated to connect Pt and the prepatterned outer pads. Finally, additional EBL and reactive ion etching were performed to eliminate the potential transport signals from MoTe₂ monolayer.

Transport Measurement

Transport measurements were conducted in a dilution refrigerator (Oxford Triton 200) with a base phonon temperature of about 10 mK. Standard low frequency (9.777 Hz) lock-in techniques with voltage preamplifier (input resistance of 100 MΩ) were used to measure the device resistance. The excitation current is 2nA to minimize sample heating.

Twist Angle Calibration

The resistance map measured as a function of top (V_{tg}) and bottom gate (V_{bg}) voltages (Extended Data Fig. 3a) was transformed into the n - D/ϵ_0 parameter space (Extended Data Fig. 3b). The carrier density n and perpendicular electric field D/ϵ_0 are defined by top and bottom gate voltages according to $n = (C_{\text{tg}}V_{\text{tg}} + C_{\text{bg}}V_{\text{bg}})/e - n_{\text{offset}}$ and $D/\epsilon_0 =$

$(C_{\text{tg}}V_{\text{tg}} - C_{\text{bg}}V_{\text{bg}})/2\epsilon_0 - D_{\text{offset}}$, where ϵ_0 , n_{offset} and D_{offset} are vacuum permittivity, intrinsic doping and built-in electric field, respectively. $C_{\text{g}} = \epsilon\epsilon_0/d_{\text{g}}$ is the gate capacitance per unit area with $\epsilon \approx 3$ and d_{g} the relative permittivity and thickness of hBN. $D_{\text{offset}} \approx 10$ mV/nm is estimated from the dual-gate map (Extended Data Fig. 3a). By finely tuning the ratio between top and bottom capacitances that align the resistance peaks parallel to the electric field axis, three most pronounced resistance peaks (indicated by black dashed lines) are clearly identified at the filling factors $\nu = -1, -2/3$ and $-1/2$. Thus, the moiré density is extracted to be $n_{\text{M}} \approx 5.85 \times 10^{12}$ cm $^{-2}$, corresponding a twist angle of $\theta = a\sqrt{\frac{\sqrt{3}}{2}}n_{\text{M}} = 4.54^\circ$, where $a = 0.352$ nm is the lattice constant for monolayer MoTe $_2$ ⁴⁵.

Single-Particle Model

The moiré Hamiltonian for the valence bands in the $\pm K$ valleys of tMoTe $_2$ was constructed in Ref^[1].

$$\hat{\mathcal{H}}_0^\tau = \begin{pmatrix} \frac{-\hbar^2(\hat{\mathbf{k}} - \tau\boldsymbol{\kappa}_+)^2}{2m^*} + \Delta_+(\mathbf{r}) & \Delta_{T,\tau}(\mathbf{r}) \\ \Delta_{T,\tau}^\dagger(\mathbf{r}) & \frac{-\hbar^2(\hat{\mathbf{k}} - \tau\boldsymbol{\kappa}_-)^2}{2m^*} + \Delta_-(\mathbf{r}) \end{pmatrix}$$

$$\Delta_\pm(\mathbf{r}) = 2V \sum_{j=1,3,5} \cos(\mathbf{g}_j \cdot \mathbf{r} \pm \psi) \pm U_z,$$

$$\Delta_{T,\tau}(\mathbf{r}) = w(1 + e^{-i\tau\mathbf{g}_2 \cdot \mathbf{r}} + e^{-i\tau\mathbf{g}_3 \cdot \mathbf{r}}), \quad (1)$$

where \mathcal{H}_0^τ is the 2×2 Hamiltonian expressed in the layer-pseudospin space, and $\tau = \pm$ is the index of $\pm K$ valleys locked to spin \uparrow and \downarrow , respectively. The layer-dependent potentials $\Delta_\pm(\mathbf{r})$ have the amplitude parameter V and phase parameters $\pm\psi$, while the interlayer tunneling $\Delta_{T,\tau}(\mathbf{r})$ has a strength parameter w . \mathbf{r} and $\hat{\mathbf{k}} = -i\partial_{\mathbf{r}}$ are the position and momentum operators, respectively. $\pm U_z$ is the layer-dependent potential induced by an external displacement field. m^* is the effective mass.

$\boldsymbol{\kappa}_\pm = [4\pi/(3a_M)](-\sqrt{3}/2, \mp 1/2)$ are located at the moiré Brillouin zone corners, and the moiré reciprocal lattice vectors $\mathbf{g}_j = [4\pi/(\sqrt{3}a_M)]\{\cos[(j-1)\pi/3], \sin[(j-1)\pi/3]\}$ with $j = 1, \dots, 6$. Here, $a_M = a/\theta$ is the moiré period and a is the monolayer lattice constant. We take the model parameters $a = 3.52$ Å, $m^* = 0.62 m_e$, $V = 11.2$ meV, $\psi = 91.0^\circ$, $w = 11.3$ meV from Ref^[4], and $\theta = 4.54^\circ$. Here m_e is the bare electron mass.

By diagonalizing Eq. (1) in the plane wave basis, we obtain the single-particle moiré

band with energy ε_{nk}^τ for the n -th band at momentum \mathbf{k} . The density of states (DOS) is then calculated by $\text{DOS}(\varepsilon_f) = \frac{1}{A} \sum_{nk\tau} \delta(\varepsilon_f - \varepsilon_{nk}^\tau)$, where A is the system area and ε_f is the Fermi energy. As we consider hole doping, the filling factor ν accounts the missing electrons per moiré unit cell and is calculated by $\nu = -A_0 \int_{\varepsilon_f}^{+\infty} \text{DOS}(\varepsilon) d\varepsilon$, where A_0 is the area of moiré unit cell. In our numerical calculation, we discretize the moiré Brillouin zone into a dense mesh of 270000 momentum points and approximate the delta function by $\delta(\varepsilon) \approx \frac{1}{\eta\sqrt{2\pi}} e^{-\frac{\varepsilon^2}{2\eta^2}}$ with the broadening parameter η to be 5 times the maximum energy level spacing in the topmost moiré band on the discretized mesh.

Exact Diagonalization Calculation

In the ED calculation, we apply a particle-hole transformation to the moiré Hamiltonian in Eq. (1) and project the many-body Hamiltonian onto the first moiré band in $+K$ valley, assuming spontaneous full valley (spin) polarization. This band is topologically nontrivial and has a Chern number of 1. We take the gate-screened Coulomb potential as the interaction, which is $V(\mathbf{q}) = \frac{2\pi e^2}{\varepsilon |\mathbf{q}|} \tanh(|\mathbf{q}|d)$ in momentum space. In the numerical calculation, we use a phenomenological dielectric constant $\varepsilon = 10$ and gate-to-sample distance $d = 10$ nm. We find that the ED spectrum is not sensitive to the variation in d . The bandwidth of the first moiré band is 33 meV at $\theta = 4.54^\circ$, while the characteristic interaction strength $\frac{e^2}{\varepsilon a_M} \approx 32$ meV. These two energy scales are comparable, placing the system in the moderate correlated regime at $\theta = 4.54^\circ$.

The states obtained in the ED spectrum are momentum eigenstates that follow the lattice translational symmetry. To construct a charge-density wave state that explicitly breaks this symmetry, we project an attractive impurity potential $\Delta(\mathbf{w}) = -\sum_{i=1}^N \delta(\mathbf{r}_i - \mathbf{w})$ onto the four-fold quasi-degenerate ground state manifold $\{|\Psi_j\rangle\}$. We choose the lowest-eigenvalue state of the projected $\Delta(\mathbf{w})$ with $\mathbf{w} = \mathbf{0}$, denoted as $|\Psi_{\text{QAHC}}\rangle$, to illustrate the charge order in the QAHC. Here $|\Psi_{\text{QAHC}}\rangle$ is a linear superposition of the four-fold quasi-degenerate ground states. The hole density shown in Fig. 3(i) is calculated with respect to $|\Psi_{\text{QAHC}}\rangle$.

Acknowledgements

X.L acknowledges support from National Key R&D Program (Grant Nos. 2024YFA1409002 and 2022YFA1403500), the National Natural Science Foundation of China (Grant Nos. 12521006 and 12274006) and Beijing National Laboratory for Condensed Matter Physics (Grant No. 2025BNLCMPKF001). M.W is supported from the National Natural Science Foundation of China (Grant No. 12404044). F.W. is

supported by National Key R&D Program (Grant Nos. 2022YFA1402400 and 2021YFA1401300) and the National Natural Science Foundation of China (Grant Nos. 12274333 and 12404084). S.L. acknowledges support from the Quantum Science and Technology – National Science and Technology Major Project (Grant No. 2023ZD0300500) and the Hong Kong RGC (Grant No. 26308524). This work is also supported by Peking Nanofab.

Author contributions

X.L. supervised the project; M.W. and L.L. fabricated the devices and performed the transport measurements with the help from Z.Z., Z.H., Q.Y.; M.W., L.L., Y.O., W.Q., F.W., and X.L. analyzed the data; Y.O., W.Q. and F.W. performed the theoretical modeling; K.W., T.T. and N.W. contributed hexagonal boron nitride materials; Y.J. and S.L. grew the MoTe₂ crystals. M.W., L.L., Y.O., W.Q., S.L., F.W. and X.L. wrote the manuscript, with the input from all others.

Competing interests

The authors declare no competing interests.

References

1. Wu, F., Lovorn, T., Tutuc, E., Martin, I. & MacDonald, A. H. Topological Insulators in Twisted Transition Metal Dichalcogenide Homobilayers. *Phys. Rev. Lett.* **122**, 086402 (2019).
2. Devakul, T., Crepel, V., Zhang, Y. & Fu, L. Magic in twisted transition metal dichalcogenide bilayers. *Nat. Commun.* **12**, 6730 (2021).
3. Li, H., Kumar, U., Sun, K., & Lin, S.-Z. Spontaneous fractional Chern insulators in transition metal dichalcogenide moiré superlattices. *Phys. Rev. Research.* **3**, L032070 (2021).
4. Reddy, A. P., Alsallom, F., Zhang, Y., Devakul, T. & Fu, L. Fractional quantum anomalous Hall states in twisted bilayer MoTe₂ and WSe₂. *Phys. Rev. B* **108**, 085117 (2023).
5. Cai, J. et al. Signatures of fractional quantum anomalous Hall states in twisted MoTe₂. *Nature* **622**, 63-68 (2023).
6. Zeng, Y. et al. Thermodynamic evidence of fractional Chern insulator in moiré MoTe₂. *Nature* **622**, 69-73 (2023).
7. Park, H. et al. Observation of fractionally quantized anomalous Hall effect. *Nature* **622**, 74-79 (2023).
8. Xu, F. et al. Observation of Integer and Fractional Quantum Anomalous Hall Effects in Twisted Bilayer MoTe₂. *Phys. Rev. X* **13**, 031037 (2023).
9. Ji, Z. et al. Local probe of bulk and edge states in a fractional Chern insulator. *Nature* **635**, 578-583 (2024).
10. Redekop, E. et al. Direct magnetic imaging of fractional Chern insulators in twisted MoTe₂. *Nature* **635**, 584-589 (2024).

11. Park, H. et al. Ferromagnetism and topology of the higher flat band in a fractional Chern insulator. *Nat. Phys.* **21**, 549-555 (2025).
12. Xu, F. et al. Interplay between topology and correlations in the second moiré band of twisted bilayer MoTe₂. *Nat. Phys.* **21**, 542-548 (2025).
13. Park, H. et al. Observation of dissipationless fractional Chern insulator. *Nat. Phys.* (2026).
14. Xu, F. et al. Signatures of unconventional superconductivity near reentrant and fractional quantum anomalous Hall insulators. Preprint at: <https://doi.org/10.48550/arXiv.2504.069727> (2025).
15. Anderson, E. et al. Trion sensing of a zero-field composite Fermi liquid. *Nature* **635**, 590-595 (2024).
16. Kang, K. et al. Evidence of the fractional quantum spin Hall effect in moiré MoTe₂. *Nature* **628**, 522-526 (2024).
17. Kang, K. et al. Time-reversal symmetry breaking fractional quantum spin Hall insulator in moiré MoTe₂. Preprint at: <https://doi.org/10.48550/arXiv.2501.02525> (2025).
18. Reddy, A. P. & Fu, L. Toward a global phase diagram of the fractional quantum anomalous Hall effect. *Phys. Rev. B* **108**, 245159 (2023).
19. Qiu, W.-X., Li, B., Luo, X.-J. & Wu, F. Interaction-Driven Topological Phase Diagram of Twisted Bilayer MoTe₂. *Phys. Rev. X* **13**, 041026 (2023).
20. Zhang, X.-W. et al., Polarization-driven band topology evolution in twisted MoTe₂ and WSe₂. *Nat. Commun.* **15**, 4223 (2024).
21. Jia, Y. et al. Moiré fractional Chern insulators. I. First-principles calculations and continuum models of twisted bilayer MoTe₂. *Phys. Rev. B* **109**, 205121 (2024).
22. Crépel, V. & Millis, A. Bridging the small and large in twisted transition metal dichalcogenide homobilayers: A tight binding model capturing orbital interference and topology across a wide range of twist angles. *Phys. Rev. Research* **6**, 033127 (2024).
23. Sheng, D. N., Reddy, A. P., Abouelkomsan, A., Bergholtz, E. J. & Fu, L. Quantum Anomalous Hall Crystal at Fractional Filling of Moiré Superlattices. *Phys. Rev. Lett.* **133**, 066601 (2024).
24. Mao, N. et al. Transfer learning relaxation, electronic structure and continuum model for twisted bilayer MoTe₂. *Commun. Phys.* **7**, 262 (2024).
25. Zhang, X.-W. et al. Twist-angle transferable continuum model and second flat Chern band in twisted MoTe₂ and WSe₂. *npj Quantum Mater.* **10**, 110 (2025).
26. Lee, M., Williams, J. R., Zhang, S., Frisbie, C. D. & Goldhaber-Gordon, D. Electrolyte Gate-Controlled Kondo Effect in SrTiO₃. *Phys. Rev. Lett.* **107**, 256601 (2011).
27. Jang, S. et al. Evolution of the Kondo lattice electronic structure above the transport coherence temperature. *Proc. Natl Acad. Sci. USA* **117**, 23467-23476 (2020).
28. Zhao, W. et al. Gate-tunable heavy fermions in a moiré Kondo lattice. *Nature* **616**, 61-65 (2023).
29. Han, Z. et al. Evidence of topological Kondo insulating state in MoTe₂/WSe₂ moiré bilayers. Preprint at: <https://doi.org/10.48550/arXiv.2507.03287> (2025).

30. Wang, L. et al. Correlated electronic phases in twisted bilayer transition metal dichalcogenides. *Nat. Mater.* **19**, 864-866 (2020).
31. Xia, Y. et al. Superconductivity in twisted bilayer WSe₂. *Nature* **637**, 833-838 (2025).
32. Pan, H. Xie, M. Wu, F. & Sarma, S. D. Topological Phases in AB-Stacked MoTe₂/WSe₂: Z₂ Topological Insulators, Chern Insulators, and Topological Charge Density Waves. *Phys. Rev. Lett.* **129**, 056804 (2022).
33. Song, X.-Y., Jian, C.-M., Fu, L. & Xu, C. Intertwined fractional quantum anomalous Hall states and charge density waves. *Phys. Rev. B* **109**, 115116 (2024).
34. Xu, C., Li, J., Xu, Y., Bi, Z. & Zhang, Y. Maximally localized Wannier functions, interaction models, and fractional quantum anomalous Hall effect in twisted bilayer MoTe₂. *Proc. Natl Acad. Sci. USA* **121**, e2316749121 (2024).
35. Perea-Causin, R., Liu, H. & Bergholtz, E. J. Quantum anomalous Hall crystals in moiré bands with higher Chern number. *Nat. Commun.* **16**, 6875 (2025).
36. Su, R. et al. Moiré-driven topological electronic crystals in twisted graphene. *Nature* **637**, 1084-1089 (2025).
37. Waters, D. et al. Chern Insulators at Integer and Fractional Filling in Moiré Pentalayer Graphene. *Phys. Rev. X* **15**, 011045 (2025).
38. Lu, Z. et al. Extended quantum anomalous Hall states in graphene/hBN moiré superlattices. *Nature* **637**, 1090-1095 (2025).
39. Abrahams, E., Kravchenko, S. V. & Sarachik, M. P. Colloquium: Metallic behavior and related phenomena in two dimensions. *Rev. Mod. Phys.* **73**, 251-266 (2001).
40. Spivak, B., Kravchenko, S. V., Kivelson, S. A. & Gao, X. P. A. Colloquium: Transport in strongly correlated two dimensional electron fluids. *Rev. Mod. Phys.* **82**, 1743-1766 (2010).
41. Sinchenko, A. A., Grigoriev, P. D., Lejay, P. & Monceau, P. Linear magnetoresistance in the charge density wave state of quasi-two-dimensional rare-earth tritellurides. *Phys. Rev. B* **96**, 245129 (2017).
42. Wang, W. et al. Correlated Charge Density Wave Insulators in Chirally Twisted Triple Bilayer Graphene. *Phys. Rev. Lett.* **132**, 246501 (2024).
43. Xie, Y. et al. Fractional Chern insulators in magic-angle twisted bilayer graphene. *Nature* **600**, 439-443 (2021).
44. Liu, F. et al. From fractional Chern insulators to topological electronic crystals in moiré MoTe₂: quantum geometry tuning via remote layer. Preprint at: <https://doi.org/10.48550/arXiv.2512.03622> (2025).
45. Kormanyos, A. et al. k · p theory for two-dimensional transition metal dichalcogenide semiconductors, *2D Mater.* **2**, 022001 (2015).

Figures

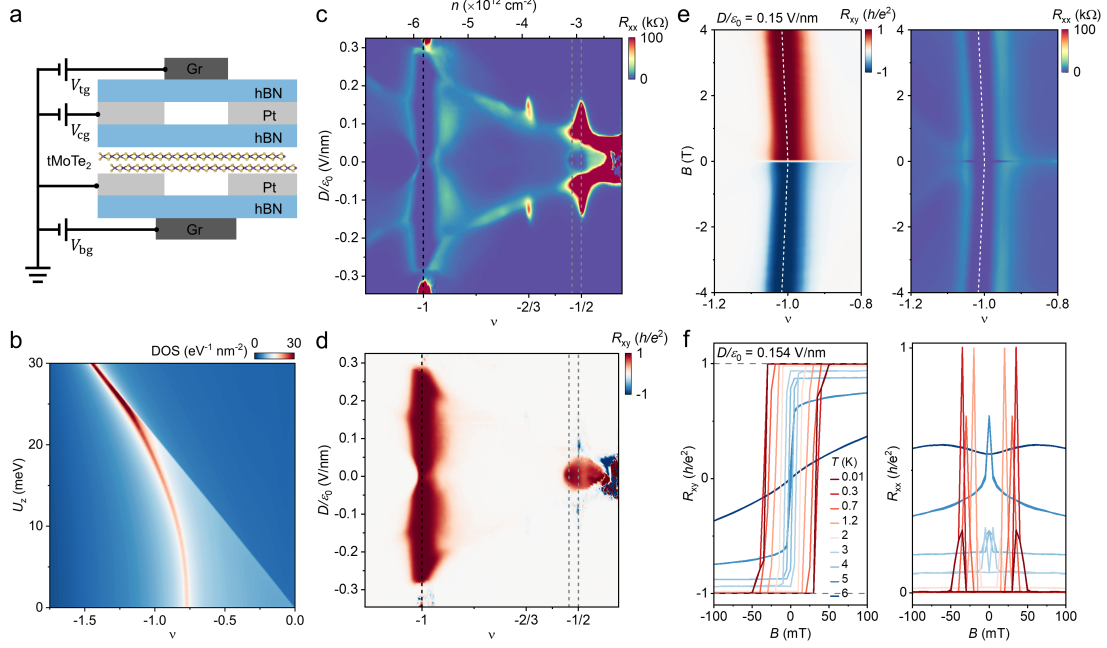


Figure 1 | Phase diagram of moiré MoTe₂. **a**, Schematic of the dual-gated tMoTe₂ device with Pt contact electrodes (light grey). Both top and bottom gates (V_{tg} and V_{bg}) are made of few-layer graphene electrodes (dark grey) and hBN dielectrics. A local Pt contact gate (V_{cg} , light grey) is used to reduce the contact resistance for low-temperature measurements. **b**, Calculated single-particle DOS for 4.54° tMoTe₂, showing a continuous shift of vHS with U_z . **c**, **d**, Electric-field- and filling-factor-dependent R_{xx} and R_{xy} at $T = 10$ mK. The corresponding carrier density (n) is shown on the top axis. R_{xx} and R_{xy} are symmetrized and antisymmetrized, respectively, using the data taken at $B = \pm 10$ mT. Black and grey dashed lines mark $\nu = -1$, -0.53 , and $-1/2$. **e**, Landau-fan diagram of R_{xy} (left) and R_{xx} (right) under $D/\epsilon_0 = 0.15$ V/nm at $T = 10$ mK. The white dashed lines correspond to an IQAH state with Chern number $|C| = 1$ at $\nu = -1$. **f**, Magnetic-field-dependent R_{xy} (left) and R_{xx} (right) measured at different temperatures under $D/\epsilon_0 = 0.154$ V/nm and $\nu = -1$. The quantized R_{xy} and concomitant minimum in R_{xx} persist up to 2 K, while the hysteresis disappears at 6 K. The grey dashed lines are to guide the eye, indicating the Hall resistance quantized at $|h/e^2|$.

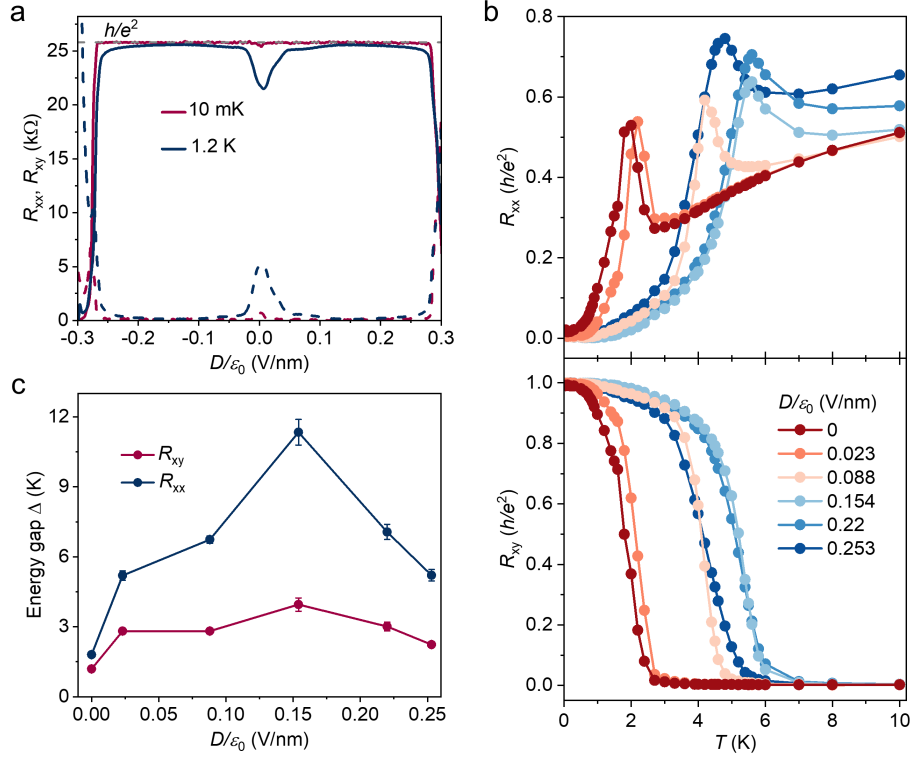


Figure 2 | Electric-field-tuned IQAH effect at $\nu = -1$. **a**, Symmetrized R_{xx} (dashed lines) and antisymmetrized R_{xy} (solid lines) as a function of D/ϵ_0 at $B = \pm 10$ mT and $T = 10$ mK (red) and 1.2 K (blue). **b**, Temperature dependence of R_{xx} (top) and R_{xy} (bottom) at selected electric fields under zero magnetic field. **c**, Energy gap as a function of electric field extracted from the data in panel **b** by using the thermal activation model (Extended Data Fig. 5). The error bars are uncertainties from the linear fits.

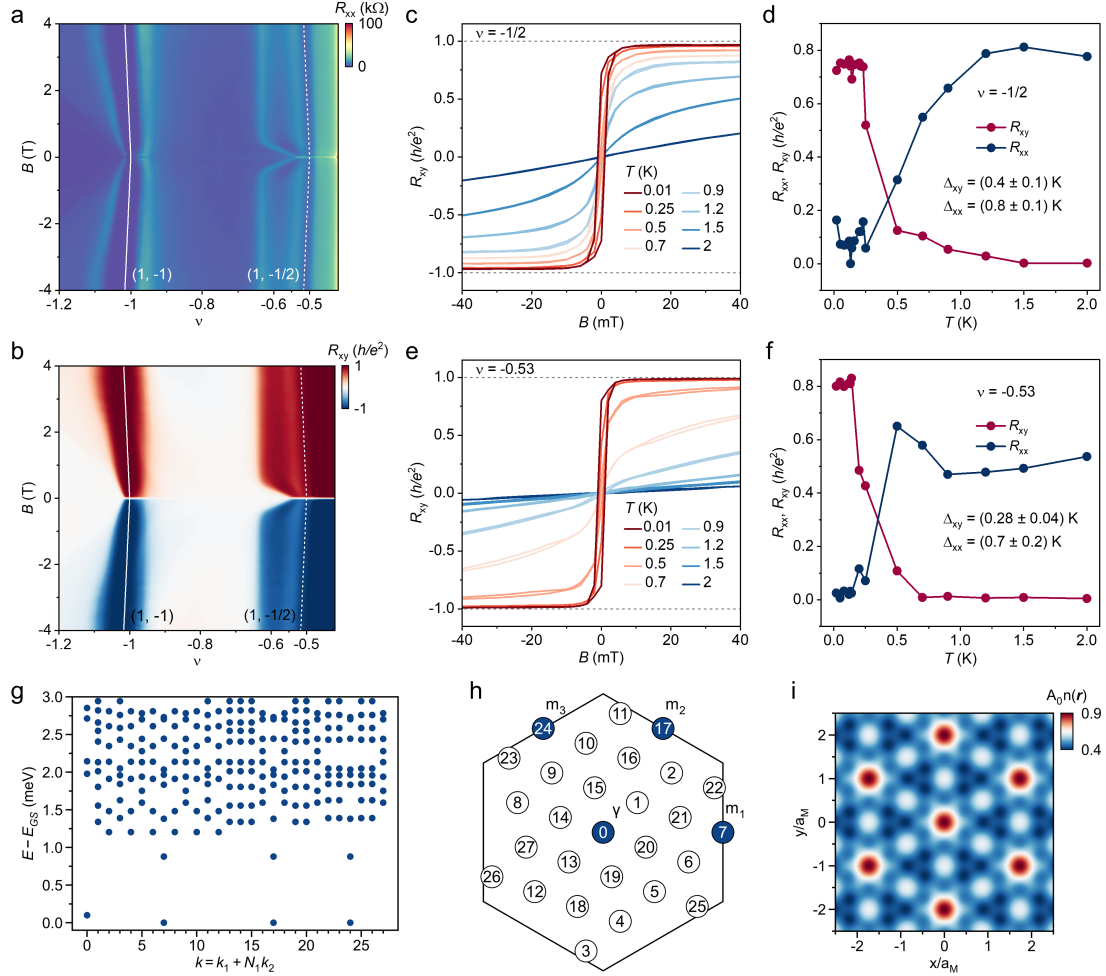


Figure 3 | Topological states at $\nu = -1/2$ and $\nu = -0.53$. **a, b**, R_{xx} and R_{xy} as functions of magnetic field and filling factor measured at $D/\varepsilon_0 = 0$ and $T = 10$ mK. The filling factors of the R_{xx} minimum (**a**) and R_{xy} maximum (**b**) disperse linearly with magnetic field, yielding slopes corresponding to Chern number $|C| = 1$ at $\nu = -1$ (white solid lines) and $\nu = -1/2$ (white dashed lines). **c, e**, Magnetic-field-dependent R_{xy} at selected temperatures with $D/\varepsilon_0 = 0$ for filling factors $\nu = -1/2$ (**c**) and $\nu = -0.53$ (**e**). Compared with $\nu = -1/2$ state, the near-quantized R_{xy} for $\nu = -0.53$ is strongly suppressed with increasing temperature at $B = \pm 10$ mT. **d, f**, Temperature dependence of the magnitudes of R_{xx} and R_{xy} at zero magnetic and electric fields. The data for R_{xy} and R_{xx} are extracted from panels **c** and **e**, as well as Extended Data Fig. 6. The energy gap determined from an Arrhenius activation model is indicated. **g**, ED energy spectrum at $\nu = -1/2$ on a 28 unit-cell cluster. The energies relative to the lowest eigenenergy are shown. **h**, The momentum-space mesh in the moiré Brillouin zone used in the ED calculations. The four quasi-degenerate ground states are located at the γ point and the three $m_{1,2,3}$ points. **i**, Hole density $n(\mathbf{r})$ of the many-body ground state pinned by an attractive impurity potential. A_0 represents the area of one moiré unit cell. Pronounced peaks appear at one quarter of MM sites on the moiré superlattice, indicating crystalline order with 2×2 enlarged unit cells.

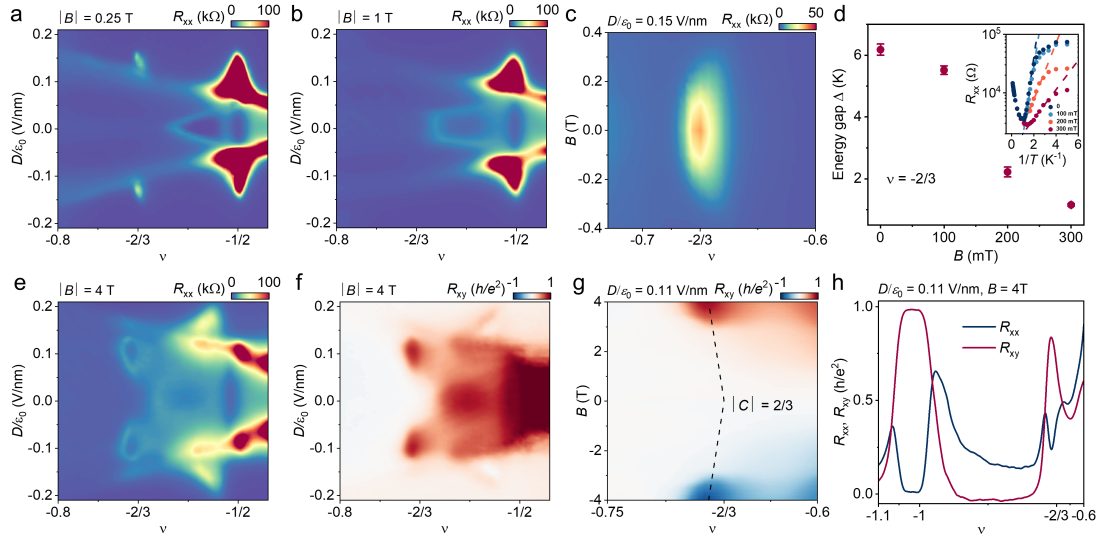
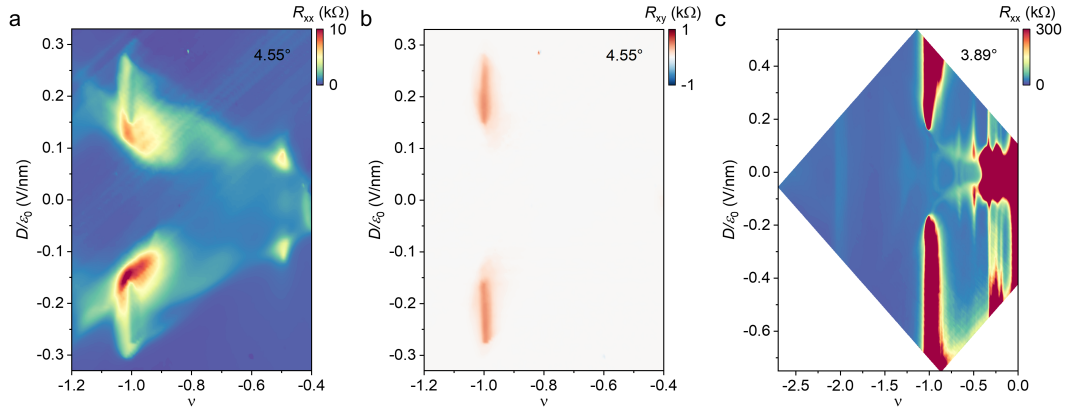
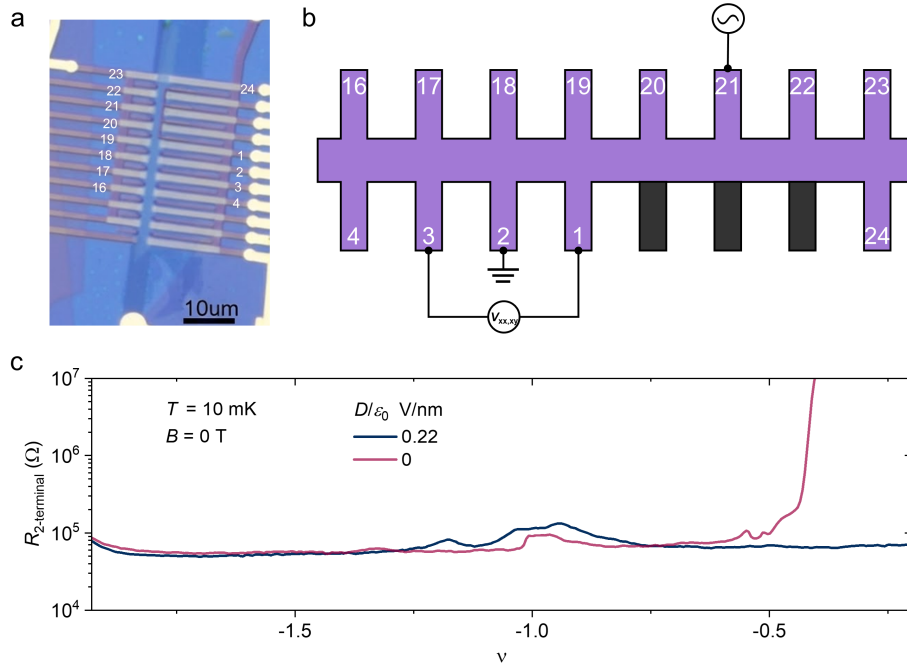


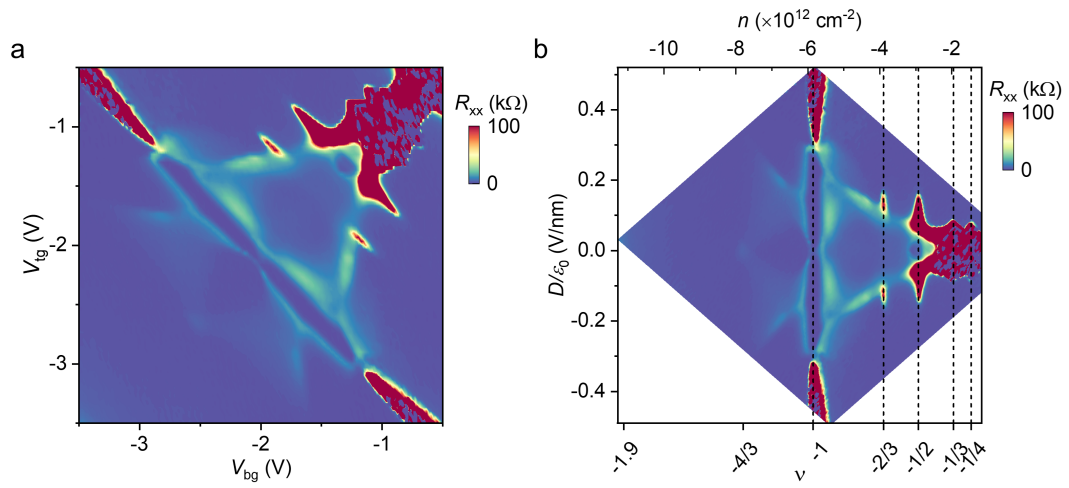
Figure 4 | Magnetic-field-induced phase transition at $\nu = -2/3$. **a, b**, R_{xx} as a function of electric field and filling factor at $|B| = 0.25$ T (**a**) and 1 T (**b**). Both the states at $\nu = -2/3$ and at $\nu = -0.53$ exhibit pronounced magnetic field dependence. **c**, Evolution of insulator-metal transition at $\nu = -2/3$ measured at $D/\epsilon_0 = 0.15$ V/nm. The correlated insulating state is observed for $|B| < 320$ mT. **d**, Magnetic-field-dependent energy gap extracted at $\nu = -2/3$ and $D/\epsilon_0 = 0.15$ V/nm. The error bars represent the fit uncertainties from Arrhenius activation model (inset). **e, f**, R_{xx} and R_{xy} as a function of electric field and filling factor at $|B| = 4$ T. **g**, Landau-fan diagram of R_{xy} measured under $D/\epsilon_0 = 0.11$ V/nm. A Chern state emerges for $B > 3$ T, and disperses linearly with magnetic field. The slope is consistent with the dashed line, corresponding to a Chern number $|C| = 2/3$ determined by the Streda formula. **h**, Line-cuts of R_{xx} and R_{xy} at $B = 4$ T extracted from **g**. All data were collected at $T = 10$ mK, except for panel **d**.



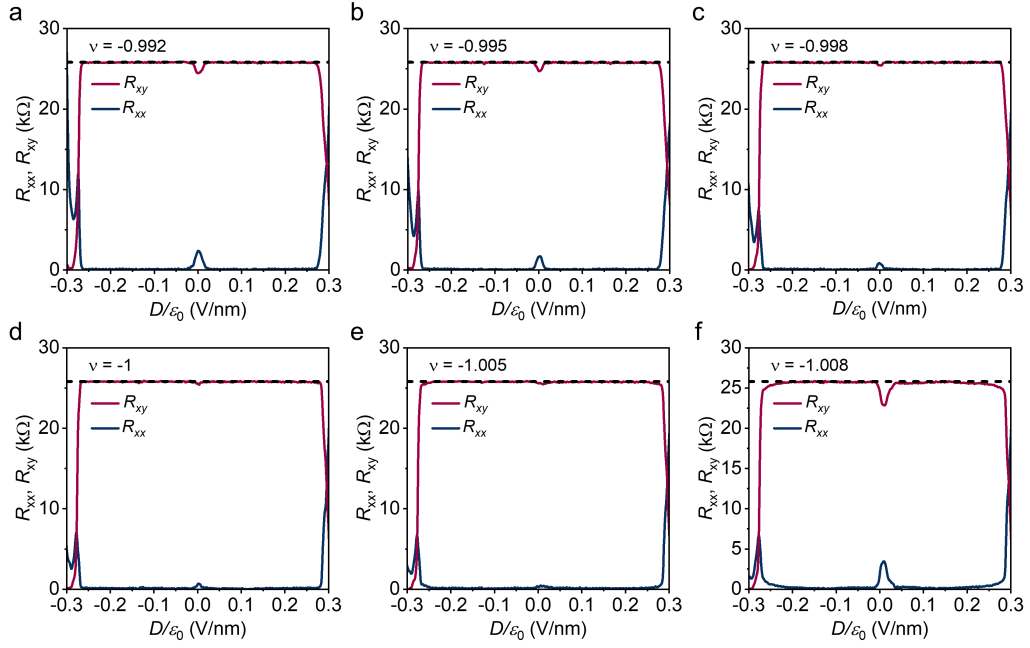
Extended Data Figure 1 | Phase diagrams of device D2 and D3 at different twist angles. a, b, R_{xx} (a) and R_{xy} (b) of device D2 ($\sim 4.55^\circ$) as a function of electric field and filling factor measured at $|B| = 0.2$ T and $T = 10$ mK. Signature of IQAH state is observed at $\nu = -1$. c, R_{xx} of device D3 ($\sim 3.89^\circ$) as a function of electric field and filling factor measured at $B = 0$ and $T = 1.5$ K. This phase diagram is consistent with previous reports^{13,14}.



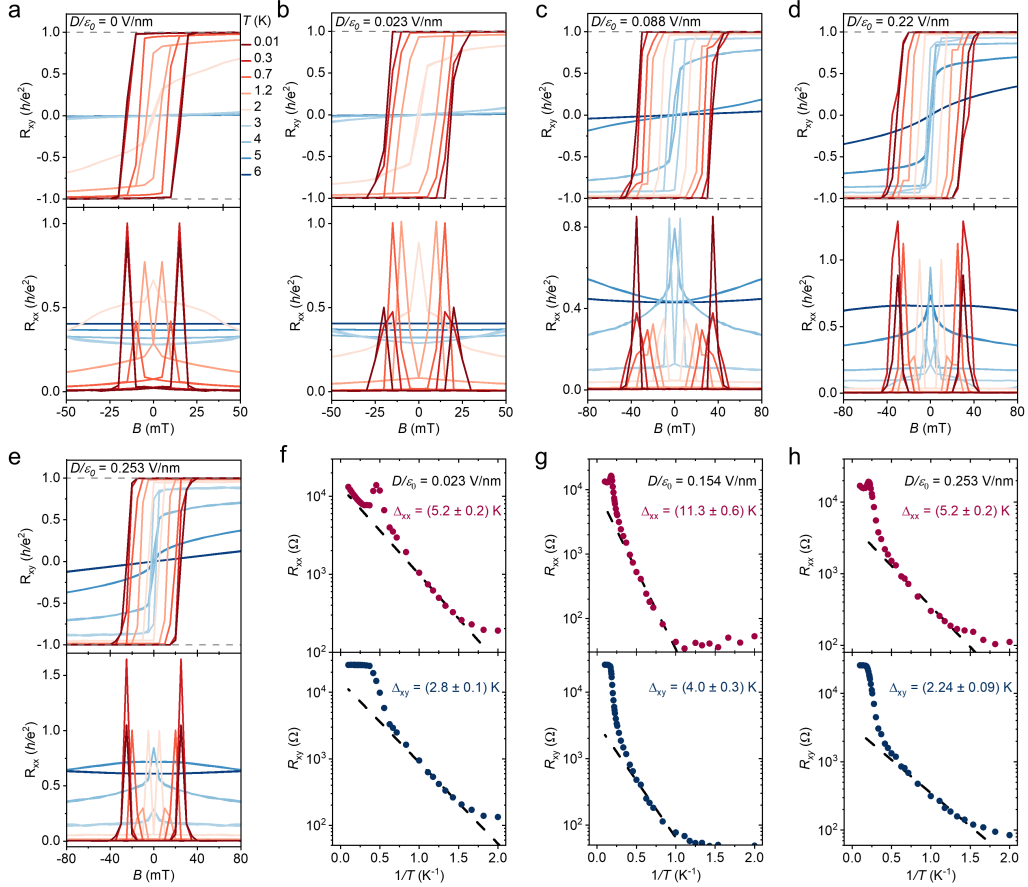
Extended Data Figure 2 | Device architecture and low-temperature transport characteristics. **a**, Optical image of the tMoTe₂ device D1. Scale bar, 10 μm. **b**, Schematic of the measurement configuration. A standard lock-in technique is employed, with an AC excitation applied between contacts 21 and 2. The voltage drop is probed between contacts 1 and 3. The three contacts shaded in black were etched. **c**, Two-terminal resistance $R_{2\text{-terminal}}$ as a function of the filling factor ν , measured at a base temperature $T = 10$ mK and zero magnetic field. Data are collected at $D/\epsilon_0 = 0.22$ V/nm (blue) and $D/\epsilon_0 = 0$ (red). The resistance was measured between contacts 1 and 3 includes the contributions from the device and the contact resistances. Outside the insulating region, the total resistance saturates around 60 kΩ, consistent with a contact resistance of approximately 30 kΩ.



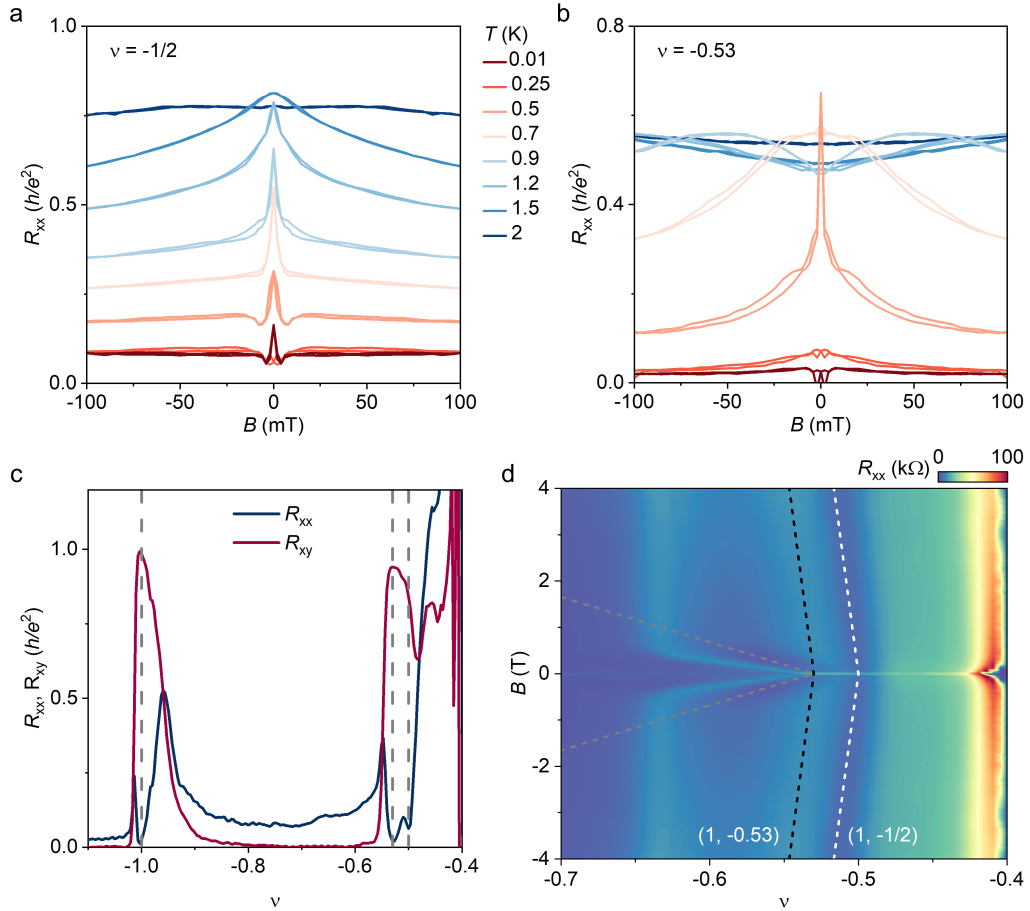
Extended Data Figure 3 | Color maps of symmetrized longitudinal resistance R_{xx} measured at $|B| = 10$ mT and $T = 10$ mK. R_{xx} is shown in $V_{bg}-V_{tg}$ (a) and $\nu-D/\epsilon_0$ (b) parameter spaces. The black dashed lines delineate the correlated insulating states identified in 4.54° tMoTe $_2$.



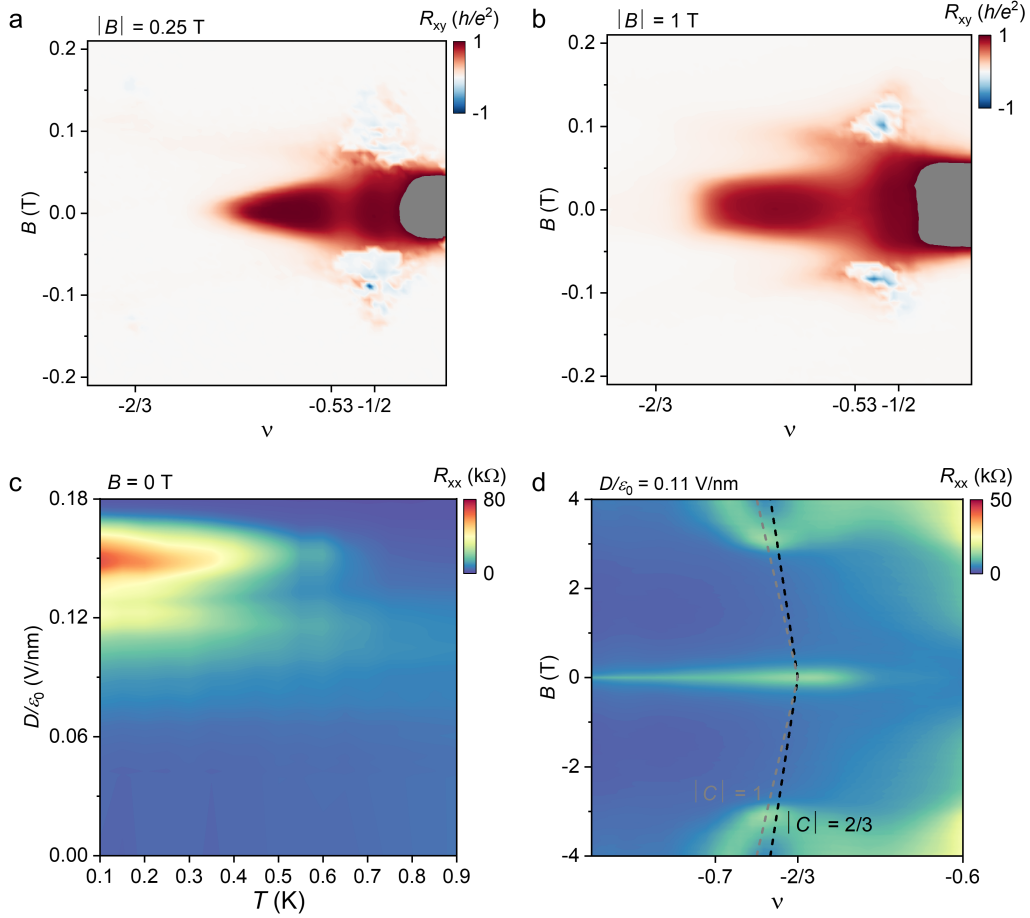
Extended Data Figure 4 | IQAH state at different filling factors near $\nu = -1$. Longitudinal resistance R_{xx} (blue) and Hall resistance R_{xy} (red) as functions of electric field measured at $T = 10$ mK for $\nu = -0.992$ (a), -0.995 (b), -0.998 (c), -1 (d), -1.005 (e) and -1.008 (f). As ν is tuned from -1 , a deviation from quantization becomes evident at zero electric field. Black dashed lines are guides to the eye. The data are symmetrized (R_{xx}) and antisymmetrized (R_{xy}) at $|B| = 10$ mT.



Extended Data Figure 5 | Temperature dependence of the IQAH state at $\nu = -1$. **a-e**, Evolution of the IQAH with temperature at selected electric fields $D/\epsilon_0 = 0$ V/nm (**a**), 0.023 V/nm (**b**), 0.088 V/nm (**c**), 0.22 V/nm (**d**), and 0.253 V/nm (**e**). **f-h**, Energy gap extracted from Arrhenius analysis at $\nu = -1$. The resistance versus inverse of temperature with linear fits (black dashed lines) at different electric fields $D/\epsilon_0 = 0.023$ V/nm (**f**), 0.154 V/nm (**g**), 0.253 V/nm (**h**). The corresponding energy gaps extracted from the fits are indicated.



Extended Data Figure 6 | Magnetic field dependence of R_{xx} measured at $D/\epsilon_0 = 0$. **a, b**, Evolution of R_{xx} at $\nu = -1/2$ (**a**) and -0.53 (**b**) with temperature. **c**, Line-cuts of R_{xx} and R_{xy} at $T = 10$ mK taken from Fig. 1d. Grey dashed lines denote $\nu = -1$, -0.53 and $-1/2$. **d**, Landau fan diagram of R_{xx} at $\nu = -1/2$ and $\nu = 0.53$ measured at $T = 10$ mK. White and black dashed lines indicate the linear dispersions in the ν - B maps for Chern number $|C| = 1$ at $\nu = -1/2$ and $\nu = -0.53$, respectively. A linear fit to $\nu = -0.53$ trajectory for $|B| < 1$ T (grey dashed line) yields a Chern number $|C| = 25$, which is inconsistent with the observed R_{xy} in Fig. 3e.



Extended Data Figure 7 | R_{xy} and R_{xx} maps measured at $T = 10$ mK. **a, b, R_{xy} as a function of ν and D/ϵ_0 at $|B| = 0.25$ T (**a**) and $|B| = 1$ T (**b**). Compared with the $\nu = -1/2$, the state at $\nu = -0.53$ displays an anomalous magnetic field dependence. The grey shadowed regions indicate the Hall resistance exceed $|h/e^2|$. **c**, Longitudinal resistance R_{xx} versus electric field D/ϵ_0 and temperature T at $\nu = -2/3$. With increasing the temperature, the correlated insulating state near $D/\epsilon_0 = 0.15$ V/nm is gradually suppressed. **d**, Longitudinal resistance R_{xx} versus magnetic field B and filling factor ν at $T = 10$ mK. The dispersion of R_{xx} minimum can be well captured by the Streda formula with $|C| = 2/3$ (black dashed line) at $\nu = -2/3$, instead of $|C| = 1$ (grey dashed line).**